Fast motion-including dose error reconstruction for VMAT with and without MLC tracking

Thomas Ravkilde[1,2], Paul J. Keall[3], Cai Grau[1,2], Morten Høyer[1,2], and Per R. Poulsen[1,2]

[1]Department of Oncology, Aarhus University Hospital, 8000 Aarhus C, Denmark

[2]Institute of Clinical Medicine, Aarhus University, 8200 Aarhus N, Denmark

[3]Radiation Physics Laboratory, Sydney Medical School, University of Sydney, NSW 2006, Australia

E-mail: thomas.ravkilde@rm.dk and per.poulsen@rm.dk.

Abstract

Purpose:

Multileaf collimator (MLC) tracking is a promising and clinically emerging treatment modality for radiotherapy of mobile tumours. Still, new quality assurance (QA) methods are warranted to safely introduce MLC tracking in the clinic. The purpose of this study was to create and experimentally validate a simple model for fast motion-including dose error reconstruction applicable to intrafractional QA of MLC tracking treatments of moving targets.

Methods:

MLC tracking experiments were performed on a standard linear accelerator with prototype MLC tracking software guided by an electromagnetic transponder system. A three-axis motion stage reproduced eight representative tumour trajectories; four lung and four prostate. Low and high modulation 6 MV single-arc volumetric modulated arc therapy (VMAT) treatment plans were delivered for each trajectory with and without MLC tracking, as well as without motion for reference. Temporally resolved doses were measured during all treatments using a biplanar dosimeter. Offline, the dose delivered to each of 1069 diodes in the dosimeter was reconstructed with 500 ms temporal resolution by a motion-including pencil beam convolution algorithm developed in-house. The accuracy of the algorithm for reconstruction of dose and motion-induced dose errors throughout the tracking and non-tracking beam deliveries was quantified.

Results:

Doses were reconstructed with a mean dose difference relative to the measurements of -0.5% (5.5% standard deviation) for cumulative dose. More importantly, the root-mean-square deviation between reconstructed and measured motion-induced 3%/3 mm γ failure rates (dose error) was 2.6%. The mean computation time for each calculation of dose and dose error was 295 ms.

Conclusions:

The motion-including dose reconstruction allows accurate temporal and spatial pinpointing of errors in absorbed dose and is adequately fast to be feasible for online use. An online implementation could allow treatment intervention in case of erroneous dose delivery in both tracking and non-tracking treatments.

Introduction

Conformal dose is a ubiquitous aim in radiotherapy (RT) in the pursuit of high and curative doses to the tumour whilst sparing healthy tissue. Volumetric modulated arc therapy (VMAT) has become a favoured treatment modality since it enables highly conformal dose delivery in an efficient way (Yu 1995, Otto 2008). Unfortunately, organ motion during treatment delivery can lead to deterioration of the dose distribution (Keall *et al* 2006, Korreman 2012). A promising method to account for the intrafraction motion is multileaf collimator (MLC) tracking, in which real-time target position monitoring is used to continuously adapt the planned MLC aperture to the position of the moving target (Keall *et al* 2001, McQuaid and Webb 2006, Liu *et al* 2009, Krauss *et al* 2011, Crijns *et al* 2012). However, while MLC tracking is now emerging in the clinic (Keall *et al* 2014), the standard premises for plan-specific quality assurance (QA) of treatments are no longer valid for MLC tracking treatments, as not all motions of the linear accelerator are known prior to treatment. Thus, an entirely new QA regime is required to safely translate MLC tracking into a clinical setting.

A failure mode and effects analysis approach to QA for MLC tracking has been performed (Sawant *et al* 2010). The highest risk failure mode identified in the MLC tracking process is that optimal leaf adaptation is not achieved. One way of testing a treatment plan's robustness to motion, with or without tracking applied, could be to deliver the plan to a phantom reproducing a large number of known or expected tumour motion trajectories and analyse the dosimetric outcome in a probabilistic manner. Another approach could be to monitor

delivered dose in real time, either through direct-readout *in vivo* dose measurements (Jarvis *et al* 2014, Mans *et al* 2010b) or real-time calculations. We have previously shown that the MLC exposure errors (Poulsen *et al* 2012a), i.e. the shielded MLC areas that should ideally be exposed and vice versa, correlate well with the transient dose errors in both tracking and non-tracking treatments (Ravkilde *et al* 2013a). However, such correlations are plan-specific and a full dose reconstruction is needed in order to robustly quantify the magnitude of the transient dose errors and to determine whether the transient errors cancel out or build up during the VMAT delivery. Previous motion-including reconstructions of actually delivered dose (Lee *et al* 2008, Bharat *et al* 2012, Poulsen *et al* 2012b, Belec and Clark 2013) have stopped short of real-time implementations in part due to the computation time, which tends to increase with increased accuracy demands. It is possible, however, that considerably less detail is actually necessary to get an indication of the dose *error*, i.e. the deviation of actual dose from planned dose, which is the main quantity of interest for patient safety during irradiation. We hypothesize that such motion-induced dose errors can be robustly reconstructed in a computationally efficient manner.

At many institutions, including our own, pre-treatment plan-specific QA is performed for challenging treatments using a homogeneous dosimeter of some kind. It is considered safe to deliver the treatment plan to a patient if the measured dose in the homogeneous phantom agrees with the planned dose, recalculated on the phantom, within some acceptable level of error. The intent of the immediate study was to provide a measure of plan deliverability similar to

this current standard that will be attainable in real time during irradiation and be able to also take into account the intrafractional motion. In this study we present a simple – but fast and scalable – motion-including dose (error) reconstruction algorithm intended for such intrafractional monitoring of dose errors. We analyse its ability to reconstruct time-resolved measurements of dose distributions and dose errors to moving targets during VMAT treatment deliveries with and without MLC tracking, and whether it is feasible for online use. An actual online application of the algorithm is considered beyond the scope of the present study.

Methods

In the following, we make use of previously published experimental dose data (Ravkilde *et al* 2013a, 2013b) for validation of a dose reconstruction algorithm, and we will therefore only briefly describe the essential parts of the experiments to make this study self-contained. We then describe in depth the algorithm developed to reconstruct the dose and dose error based on experiments, as well as the comparison of measured and reconstructed dose data.

Experiments and data processing

MLC tracking experiments were carried out at Aarhus University Hospital on a Trilogy linear accelerator equipped with a 120 leaf Millennium MLC (Varian Medical Systems, Palo Alto, CA) connected to a prototype MLC tracking system (Sawant *et al* 2008). The system was guided by the real-time 3D target position

signal of an electromagnetic transponder at 30 Hz (Ravkilde *et al* 2011) [RayPilot, Micropos Medical, Sweden]. Time-resolved dose distributions were measured at 72 Hz with a biplanar diode arrays dosimeter (Bedford *et al* 2009) [Delta4PT, Scandidos, Sweden; hereafter "the phantom"] that was placed on an in-house modified (Ravkilde *et al* 2013b) programmable motion stage (Malinowski *et al* 2007). The motion stage reproduced eight patient-measured tumour trajectories representing different motion patterns (Keall *et al* 2011); four lung trajectories ("Typical" motion, High-frequency breathing, Predominantly left-right motion, and Baseline shifts) and four prostate trajectories (Continuous drift, Persistent excursion, Transient excursion, and High-frequency excursions). For the lung trajectories, prediction was used to compensate for the 140 ms tracking system latency (Ravkilde *et al* 2011). For each trajectory, two 6 MV 358° single-arc RapidArc VMAT plans (one low and one high modulation) were delivered to the phantom (Ravkilde *et al* 2013a, Poulsen *et al* 2012a). The VMAT treatments were delivered for each trajectory with and without MLC tracking, as well as to a static phantom for reference. Treatment times, monitor units (MU), and results of dose measurements have been described in our previous work (Ravkilde *et al* 2013a).

After completion of the experiments, Dynalog MLC log files (Litzenberg *et al* 2002) and tracking log files from the tracking program were collected and synchronized to the time-resolved dose data measurements. To facilitate direct comparison of the time-resolved doses between different experiments (e.g. with and without motion), the dose measurements were down-sampled from steps with equal duration (13.9 ms) to steps of 100 dose pulses (mean temporal

resolution of 499 ms [standard deviation: SD=75 ms]). The same step size was used in the dose reconstruction.

Dose reconstruction algorithm

A simple dose reconstruction algorithm was implemented in Matlab version R2011a (The Mathworks Inc., MA) for offline reconstruction of the time-resolved evolution of dose distributions. The algorithm builds upon a simplified version of the pencil beam convolution (PBC) algorithm by Storchi and collaborators (Storchi *et al* 1999, Storchi and Woudstra 1996, 1995), which is implemented in a slightly modified version in the Eclipse treatment planning system (TPS) [Varian Medical Systems]. In their PBC algorithm the dose in a voxelized water equivalent block is calculated in at least five planes at different depths by convolution of single pencil beam (SPB) 2D scatter kernels with a normalized fluence, and converted to other depths by interpolation of percentage depth dose (PDD) along the ray lines and by inverse square law scaling.

Realizing that the most computationally intensive parts of this PBC algorithm are convolutions and ray tracing, we have simplified these two parts in our algorithm. Firstly, a relative lateral dose distribution is computed from convolution of the normalized fluence with the scatter kernel in one plane; the isoplane, rather than five planes. Secondly, rather than calculating the dose to a full 3D grid of voxels, many of which may not be needed, the algorithm calculates the dose in an arbitrary set of points defined by the user. This has several

benefits, the most obvious being that the calculation can be restricted to the points needed. In addition to this, utilizing that the phantom is homogeneous, no discretization of voxels exist and no ray tracing is needed to calculate the dose. Furthermore, the position of the calculation points may be adjusted individually throughout treatment, effectively mimicking motion, rotation and/or deformation. Thus, it is a more general description in the sense of calculation points and motion but not in the sense of density changes.

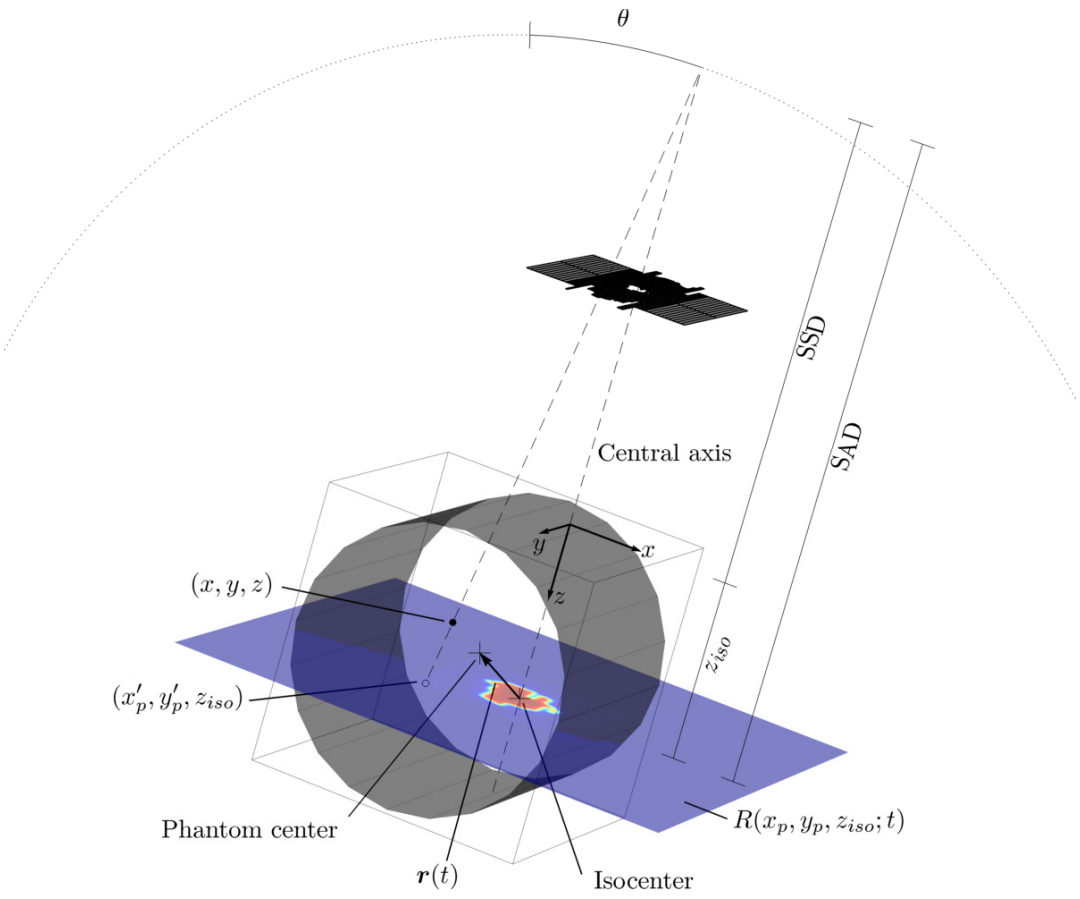

Figure 1 Schematic representation of the reconstruction model (not to scale). The cylindrical phantom is outlined with grey patches. The surrounding box illustrates the effect of neglecting the phantom surface obliquity. At time $\boldsymbol{t}$ a calculation point $(\boldsymbol{x}, \boldsymbol{y}, \boldsymbol{z})$ within the phantom is projected onto the isoplane at $(\boldsymbol{x'_p}, \boldsymbol{y'_p}, \boldsymbol{z_{iso}})$, taking into account the displacement $\boldsymbol{r(t)}$ of the phantom centre from the isocenter. The MLC is shown in grey and the resulting relative dose in the isoplane $\boldsymbol{R(x_p, y_p, z_{iso}; t)}$ is shown as a colour

wash. The gantry is rotated $\boldsymbol{\theta}$ degrees. The source-to-axis distance (SAD), source-to-surface distance (SSD), and the depth of the isoplane $\boldsymbol{z_{iso}}$ are also shown for completeness.

Figure 1 shows a schematic representation of the model for the fast motion-including (FMI) dose reconstruction. Calculation points can be chosen arbitrarily within the phantom and are shifted according to the current phantom position measurement $\boldsymbol{r}(t)$ in order to model translational motion. For a calculation point (x, y, z) the projected point on the isoplane is

$$\left(x'_p, y'_p, z_{iso}\right) = \left(x\frac{\mathrm{SAD}}{\mathrm{SSD}+z}\ , y\frac{\mathrm{SAD}}{\mathrm{SSD}+z}\ , z_{iso}\right),$$

where the source-axis distance SAD = 100 cm is the distance between the beam source and the isoplane and the source-surface distance SSD is the distance between the source and the phantom surface. The dose delivered at (x, y, z) in an infinitesimal time interval dt at time t is calculated as

$$D(x, y, z; t) = R\left(x'_p, y'_p, z_{iso}; t\right) \cdot D_a(z; t) \cdot \dot{M}\ dt \cdot c_d(z) \cdot c_\theta\ ,$$

where $R\left(x_p, y_p, z_{iso}; t\right)$ is relative dose in the isoplane (dimensionless), $D_a(z; t)$ is absolute depth dose on the central axis of a beam calibration field (units Gy/MU), $\dot{M}$ is the dose rate (units MU/s), $c_d(z)$ is a density correction factor (dimensionless), and c_θ is a gantry dependent attenuation correction factor due to material between the beam source and the phantom (couch etc.) [dimensionless]. Each of these factors will be described in detail below.

The relative isoplane dose is calculated for each point in time by convolution of the field intensity function with a pencil beam kernel:

$$R\left(x_p, y_p, z_{iso}; t\right) = F\left(x_p, y_p; t\right) * K(x_p, y_p).$$

The field intensity function $F(x_p, y_p; t)$ describes the field shape and blocking in the field at time t and takes values of 1 in an open beam, 0 behind collimator jaws, and 0.019 for points shielded only by MLC leaves. The leaf transmission factor of 0.019 for these 6 MV beams was taken from the Eclipse TPS at our clinic. The kernel matrix $K(x_p, y_p)$ was constructed from a rotation symmetric SPB kernel (Storchi *et al* 1999) extracted from the TPS. While the SPB kernels were available for five different depths (1.5, 5, 10, 20 and 30 cm) only the kernel at 10 cm depth was used, that being approximately the radius of the cylindrical Delta4PT phantom (11 cm) and thus also the approximate depth of the isoplane z_{iso} for a static phantom. The SPB kernel radius was truncated from 28 cm to 2.5 cm to allow faster computation. The truncation removed 0.5% of the area under the kernel. The intensity profile of the beam was assumed completely flat.

Scaling to absolute dose and to other depths than the isoplane was done by multiplication with a single measured PDD in water for a 10×10 cm^2 field, which was renormalized to absorbed dose per MU according to beam calibration and corrected for changing SSD:

$$D_a(z;t) = \mathrm{PDD}_{norm}(z) \cdot c_M(z;t) \cdot c_i(t)$$

$$\mathrm{PDD}_{norm}(z) = \frac{1\ \mathrm{Gy}}{100\ \mathrm{MU}} \frac{\mathrm{PDD}(z)}{\mathrm{PDD}(z_{cal})}$$

$$c_M(z;t) = \left(\frac{\mathrm{SSD} + z_{cal}}{\mathrm{SSD}_{cal} + z_{cal}} \frac{\mathrm{SSD}_{cal} + z}{\mathrm{SSD} + z}\right)^2$$

$$c_i(t) = \left(\frac{\mathrm{SSD}_{cal} + z_{cal}}{\mathrm{SSD} + z_{cal}}\right)^2$$

$$\mathrm{SSD} = \mathrm{SSD}_{static} + r_z(t).$$

Here $c_M(z;t)$ is Mayneord's *F* factor (Mayneord and Lamerton 1941) and $c_i(t)$ is an inverse square law correction factor, both taking into account the position of the moving phantom by the z-component $r_z(t)$ of the phantom displacement vector $\boldsymbol{r}(t)$. The measured PDD curve was obtained from commissioning data files for the TPS. At our institution, the beam is calibrated to 1 Gy per 100 MU at depth $z_{cal} = 5$ cm for $\mathrm{SSD}_{cal} = 95$ cm with a 10×10 cm^2 field. With the phantom centre aligned with the isocenter the source-surface distance is $\mathrm{SSD}_{static} = 89$ cm.

Since the Delta4PT phantom is not made of water, we applied a density correction factor using the equivalent path length (or effective depth, z_{eff}) method;

$$c_d(z) = \frac{\mathrm{PDD}(z_{eff})}{\mathrm{PDD}(z)}\left(\frac{\mathrm{SSD} + z_{eff}}{\mathrm{SSD} + z}\right)^2$$

$$z_{eff} = z \cdot \rho_e,$$

where ρ_e is the electron density of the medium (PMMA in this case) relative to water as determined by Thomas (1999). The CT image used in the TPS revealed a density of the Delta4PT phantom of 217 HU, corresponding to an electron density of 1.11 relative to water.

At posterior gantry angles the entrance beam passed through the couch, the RayPilot couch top, and the motion stage platform carrying the Delta4PT phantom (Ravkilde *et al* 2013b). The total attenuation of these objects was measured as a function of gantry angle θ for the central diode in the phantom

and used as a common gantry dependent correction factor c_θ for all points in the reconstructed dose. The angle dependency of the diodes is corrected for in the measurements by the Delta4PT software.

No corrections were done for the surface obliqueness of the phantom, as illustrated by the cube surrounding the phantom in Figure 1.

Comparison with measurements

Dose

The difference between the FMI reconstructed dose and the measured dose was calculated for each diode at each point in time, and its mean (and SD) over all diodes and times was reported. The dose difference was calculated relative to the maximum dose for each corresponding point in time in the measured static reference. Positive values correspond to overestimation of doses by FMI and negative values to underestimation. Detectors with final accumulated doses below 5% of the maximum accumulated dose in the measured static reference were excluded in the calculations.

Motion-induced dose error

For each plan, each of the measured dose distributions delivered during motion were first compared with the measured static reference dose distribution at each point in time using a γ-test (Low *et al* 1998) with the global 3%/3 mm criteria also used for daily QA in our clinic. Then, each of the FMI reconstructed dose distributions during motion were similarly compared with the FMI

reconstructed static reference dose distribution at each point in time using a 3%/3 mm γ-test. Finally, the root-mean-square (rms) deviation between the time-resolved measured and reconstructed motion-induced γ failure rates was found. The time-resolved γ-test was developed in-house (Ravkilde *et al* 2013a) and optimized specifically for the Delta4PT geometry (combined 2D γ-tests for the two detector planes, similar to the calculations by the commercial Delta4PT software when using a previous measurement as reference). Similar to the comparison of measured and reconstructed doses, the percentage dose difference inherent in the γ-test was calculated relative to the maximum dose for each corresponding point in time in the measured static reference. Again, detectors with final accumulated doses below 5% of the maximum accumulated dose in the measured static reference were excluded. To quantify how robustly the FMI reconstruction estimated whether dose errors were above or below some pre-defined action level, a sensitivity analysis was performed based on the action level of 10% γ failure also used in the daily QA in our clinic.

Results

Dose

Averaging over all experiments, diodes, and time points, the measured doses were reconstructed with a mean dose difference of -0.6% (SD=8.1%) for transient doses and -0.5% (SD=5.5%) for cumulative doses. For the accumulated doses over the complete arc fields, doses were reconstructed with a mean dose difference of -1.1% (SD=5.2%). Table 1 compiles the results stratified into

intensity modulation complexity and static, motion without tracking, or motion with tracking, while Figure 2 shows the distribution of dose differences as a function of relative doses for all experiments, diodes, and time points.

Table 1 Mean (and standard deviation) of dose differences between reconstructed and measured time-resolved dose distributions. Unit: % of max dose.

Plan	Static	No tracking	Tracking	All
Transient				
Low modulation	-0.2 (7.7)	-0.2 (8.6)	-0.22 (8.0)	-0.6 (8.1)
High modulation	-0.8 (8.0)	-0.9 (8.0)	-0.8 (8.2)	
Cumulative				
Low modulation	0.2 (6.0)	0.3 (5.9)	0.3 (6.1)	-0.5 (5.5)
High modulation	-1.0 (5.8)	-1.0 (5.0)	-0.9 (5.0)	
Accumulated				
Low modulation	-0.4 (5.4)	-0.4 (5.4)	-0.4 (5.4)	-1.1 (5.2)
High modulation	-1.7 (5.7)	-1.8 (4.8)	-1.5 (4.8)	

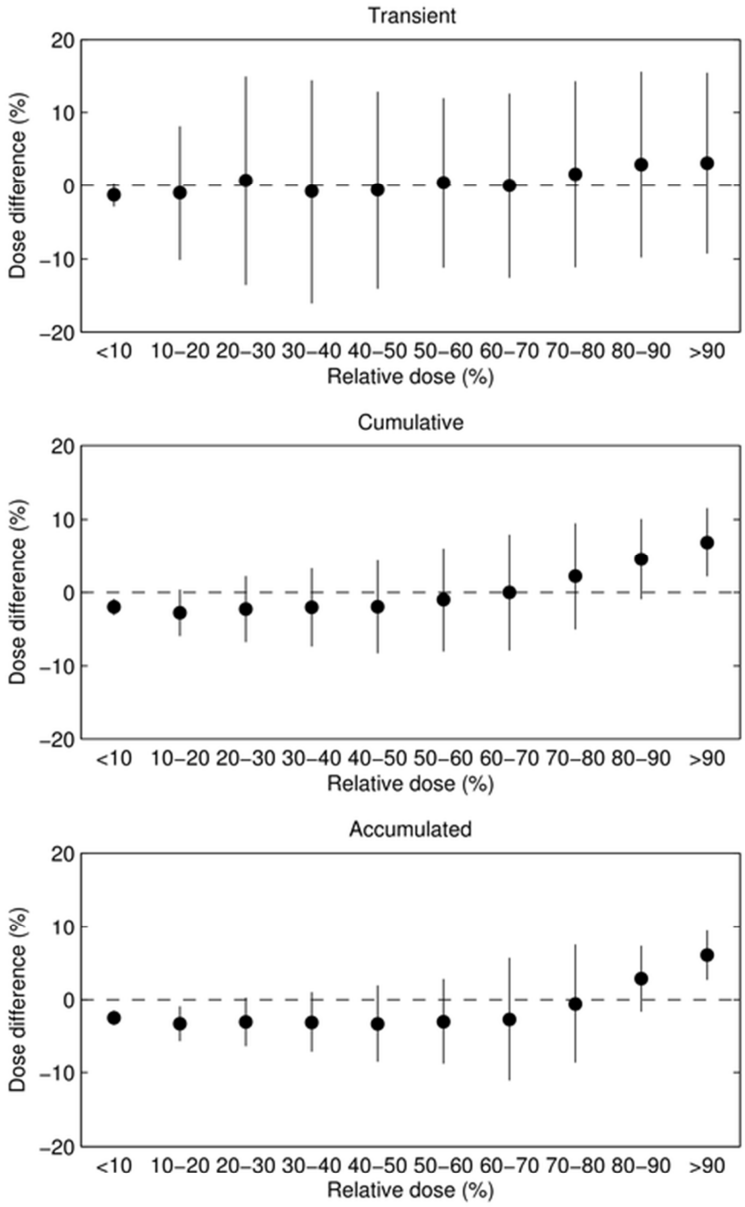

Figure 2 Mean (dots) and standard deviation (vertical line segments) of the dose differences between reconstructed and measured doses shown as a function of relative dose. Relative doses of all time points were divided into bins of 10%. A dashed horizontal line marks the level of no difference.

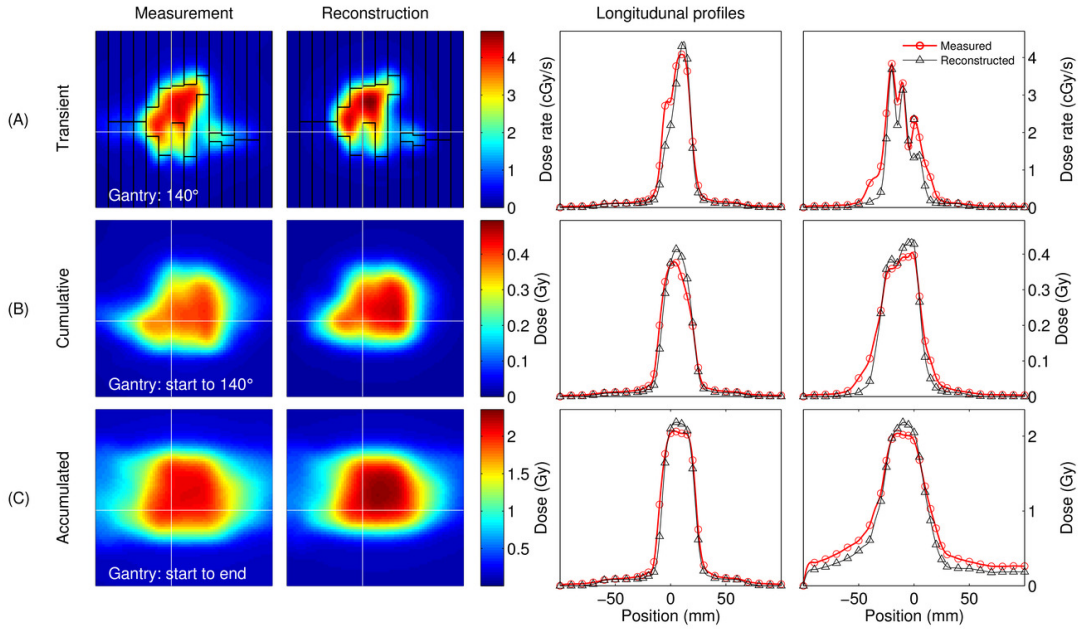

Figure 3 Comparison of measured and reconstructed doses for high modulation VMAT of a lung tumor travelling along the Baseline shifts motion trajectory without MLC tracking. Left: 2D measured and reconstructed dose distributions in a detector plane. Right: dose profiles for the measured (thick curves) and reconstructed (thin curves) doses along the white lines marked on the 2D dose distributions. Circles mark the actual diode measurements and triangles the reconstructed doses in the diode points. Lines mark interpolated values (cubic spline). Row (A): transient doses for a time interval of 0.5 seconds at gantry angle 140° with overlay showing the MLC aperture. Row (B): cumulative doses at gantry angle 140°. Row (C): final accumulated doses. The time of 140° gantry angle is marked as a dashed vertical line in Figure 4.

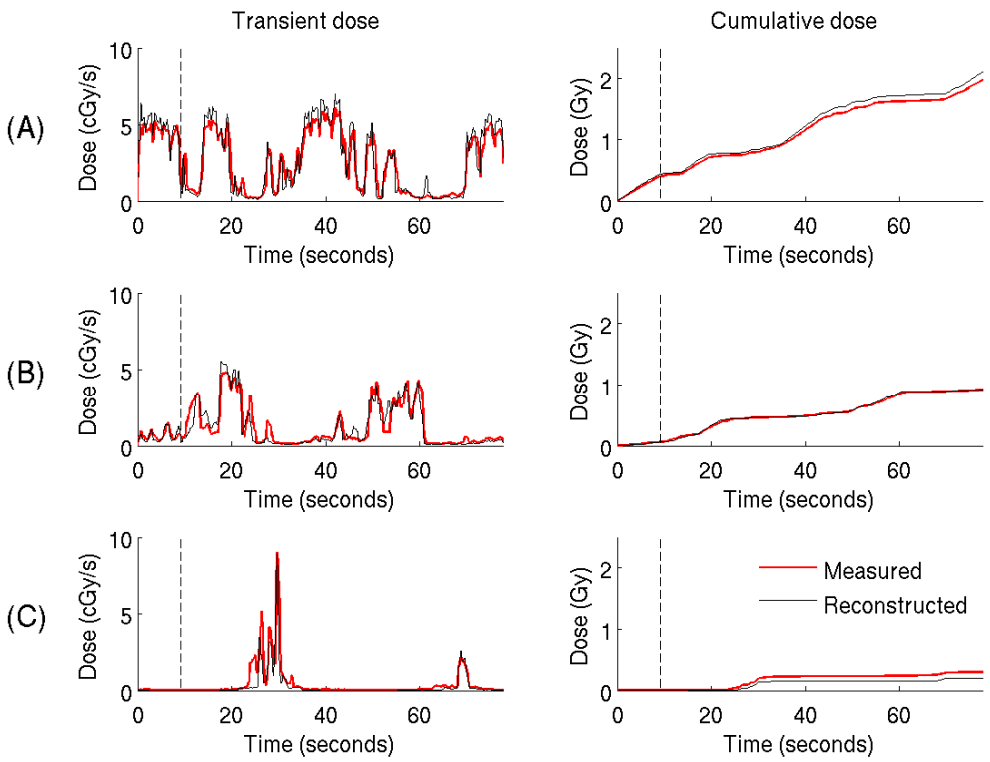

Figure 4 Measured (thick curves) and reconstructed (thin curves) doses to three sample diodes in the phantom for high modulation VMAT of a lung tumor travelling along the Baseline shifts motion trajectory without MLC tracking; (A) the diode in the center of phantom, (B) a diode in a high dose gradient, and (C) a diode in the periphery of the phantom. Transient doses are shown in the left column and the resulting cumulative doses in the right column. The dashed vertical lines mark the time of the doses shown in Figure 3 rows (A) and (B).

The reconstruction predominantly underestimated doses in low dose regions and overestimated doses in high dose regions (Figures Figure 2-Figure 3). There was in general good agreement between reconstructed and measured doses in the high dose gradient regions (Figure 3), although with a generally higher spread in the intermediate dose range of the penumbra than in the low and high dose ranges (Figure 2). Altogether this indicates that the overall shapes of the reconstructed doses were well reconstructed, while the reconstruction did

not perform as well at dose plateaus. The temporal evolution of dose was also well reconstructed, as illustrated by the synchrony of the measured and reconstructed transient dose curves in Figure 4.

The mean computation time was 35.9 ms (SD=2.0 ms) for each transient dose distribution calculation in Matlab (1069 diode points) including overhead on a standard laptop equipped with an Intel® Core™ i5-M460 CPU running at 2.53 GHz. Computation times of the FMI dose reconstruction scaled sublinearly with the number of calculation points.

Motion-induced dose error

The dose distributions of the moving phantom were compared with the static reference dose distribution to quantify the motion-induced dose errors in both experiments and in the reconstructions hereof (illustrated in Figure 5). Although the FMI dose error reconstructions indicate patterns of erroneous dose deposition, dose error distributions were reconstructed with some uncertainty for transient doses (Figure 5). For cumulative and final accumulated doses, however, the spatial distribution of measured dose errors were well reconstructed, allowing pinpointing positions of erroneous dose deposition throughout beam delivery. The resulting γ failure rates for the high modulation VMAT plans are shown in Figure 6 and Figure 7. The γ failure rates of all experiments and the reconstructions thereof are summarized in the scatter plots in Figure 8.

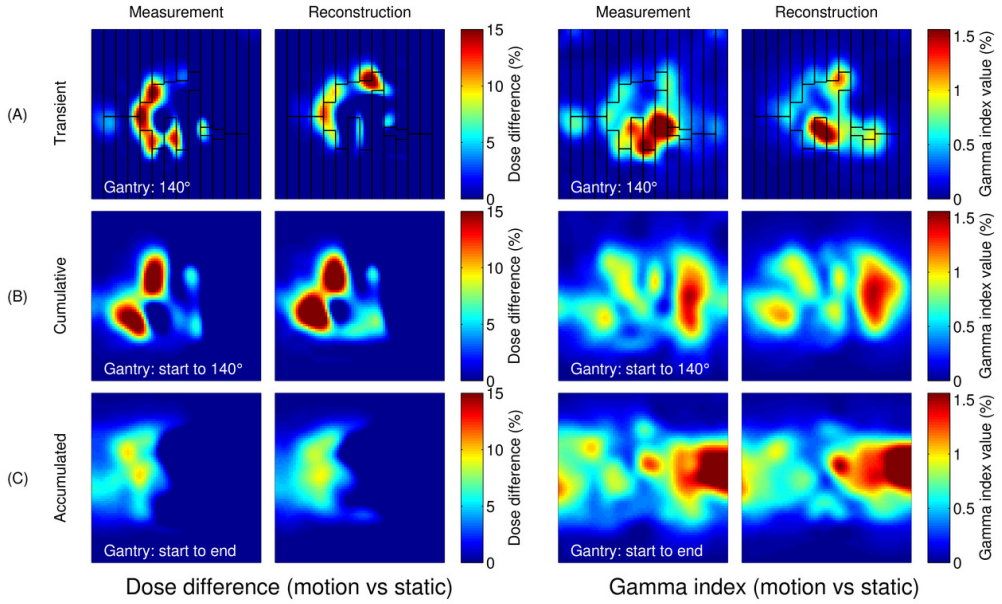

Figure 5 Comparison of measured and reconstructed 2D distributions of motion-induced dose errors in a detector plane for high modulation VMAT of a lung tumor travelling along the Baseline shifts motion trajectory without MLC tracking (same experiment at the same time points as in Figure 3). Left: dose differences. Right: γ index maps. Row (A): transient doses for a time interval of 0.5 seconds at gantry angle 140° with overlay showing the MLC aperture. Row (B): cumulative doses at gantry angle 140°. Row (C): final accumulated doses.

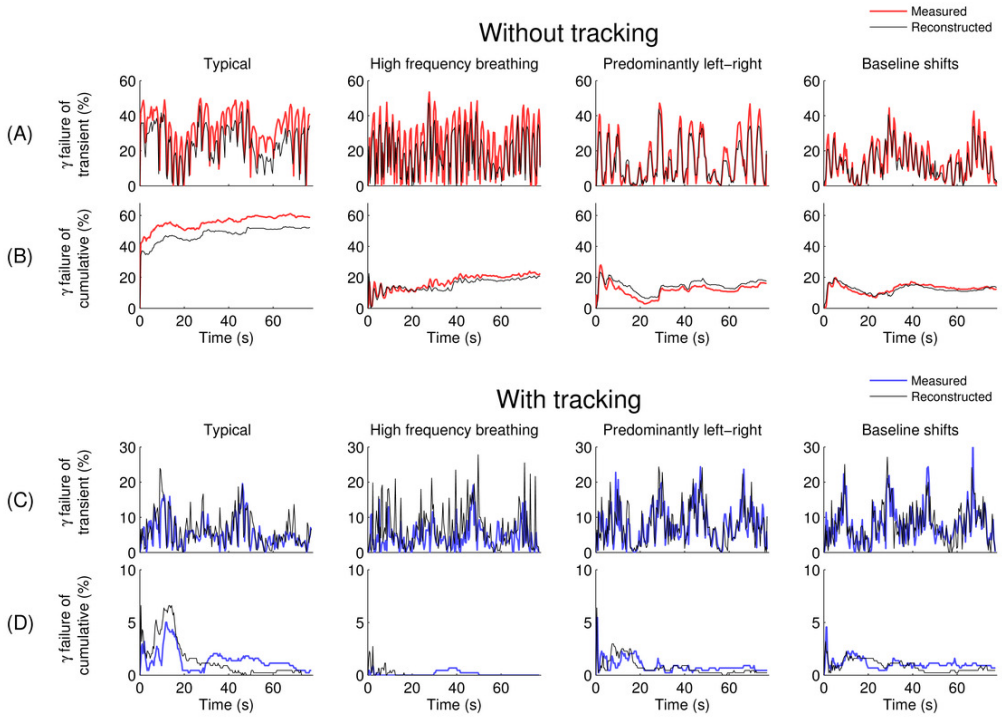

Figure 6 Comparison of measured (thick curves) and reconstructed (thin curves) 3%/3 mm γ failure rates during the high modulation VMAT deliveries to a lung tumour travelling along each of the lung tumour motion trajectories without (top panel) and with (bottom panel) tracking. The γ failure rate is shown for both transient doses (rows (A) and (C)) and cumulative doses (rows (B) and (D)). Note the different γ-scales between rows.

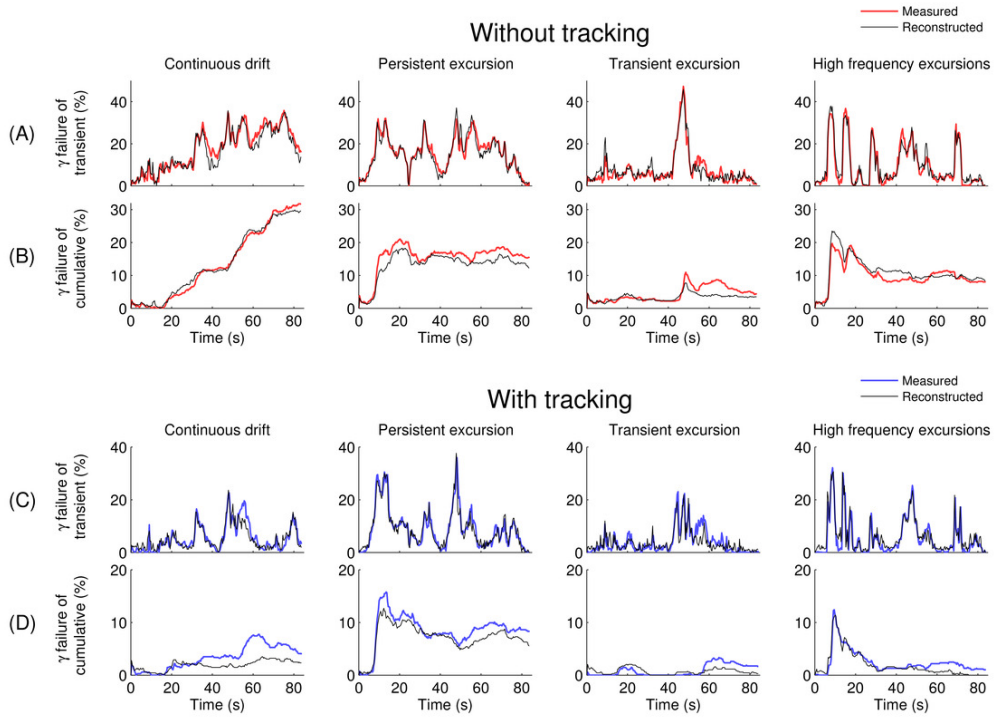

Figure 7 Comparison of measured (thick curves) and reconstructed (thin curves) 3%/3 mm γ failure rates during the high modulation VMAT deliveries to a prostate tumour travelling along each of the prostate motion trajectories without (top panel) and with (bottom panel) tracking. The γ failure rate is shown for both transient doses (rows (A) and (C)) and cumulative doses (rows (B) and (D)). Note the different y-scales between rows.

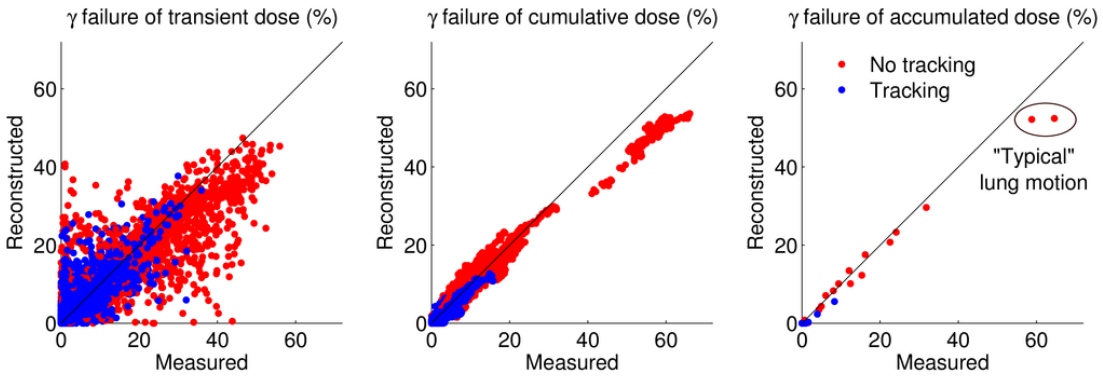

Figure 8 Scatter plots of reconstructed vs. measured 3%/3 mm γ failure rates for transient, cumulative, and accumulated doses. The line of unity is shown for reference.

Some uncertainty was present in the reconstruction of transient dose errors (Figure 8 left), but the transient errors tended to average out in the cumulative dose errors (Figure 8 middle). For all motion experiments, both with and without tracking, the γ failure rates were well reconstructed for cumulative dose errors throughout beam delivery, and hence also for final accumulated dose errors. Only the "Typical" lung tumour trajectory delivered without tracking had considerable discrepancy between measured and reconstructed motion-induced γ failure rates (Figure 8 right). This was the case for both high and low modulation VMAT plans. The discrepancy was a result of a systematic underestimation of the transient γ failure rate in the reconstruction (Figure 6 row (A), first column) caused by a range of diodes that just fulfilled the 3%/3 mm criterion in the reconstruction while they just failed the criterion in the experiments. This led to an underestimation of the cumulative dose error throughout beam delivery (Figure 6 row (B), first column). For these two cases, both measured and reconstructed cumulative dose errors were above 40% γ failure throughout most of the beam delivery.

Averaging over all experiments, the rms deviations between reconstructed and measured motion-induced γ failure rates were 6.3% (transient dose), 2.6% (cumulative dose), and 2.7% (accumulated dose). Assuming an action level of 10% γ failure in cumulative dose, the sensitivity (fraction of true positives) of the FMI dose error reconstruction was 93.0% and the specificity (fraction of true negatives) was 97.5%. The false positives (i.e. the 7% cases with a cumulative γ failure rate below 10% despite the FMI dose error reconstruction

predicting a γ failure rate above 10%) had a median γ failure rate of 11.2%. The false negatives (i.e. the 2.5% cases with γ failure rate above 10% despite the FMI dose error reconstruction predicting a γ failure rate below 10%) had a median γ failure rate of 9.4%.

The mean computation time was 259.4 ms (SD=9.5 ms) for each transient or cumulative γ-test including overhead for a mean of 535 (SD=140) calculation points.

Discussion

The FMI algorithm for motion-including dose (error) reconstruction was demonstrated and experimentally validated in two orthogonal planes for complex rotational RT treatments delivered to a moving phantom with and without MLC tracking. The algorithm was created in order to allow real-time monitoring of dose deposition to moving targets during radiotherapy treatments with possible intervention in case of gross treatment errors. The FMI algorithm reconstructed motion-induced γ failure rates with 2.6% (cumulative dose) and 2.7% (accumulated dose) rms deviation of measured values. These results are comparable to reconstructions of the same experiments using a TPS and motion-mimicking treatment plans, which achieved a rms deviation of 1.5% for accumulated doses (Ravkilde *et al* 2013b). The higher deviation using FMI dose error reconstruction is mainly due to the two non-tracking lung VMAT plan deliveries to the phantom reproducing the “Typical” lung tumour trajectory. Both of these had γ failure rates in cumulative dose exceeding 40% (substantially

higher than any other delivery) for both measured and reconstructed doses. This is much higher than the action level of 10% γ failure taken from the daily QA protocol at our clinic and used in the sensitivity analysis. High sensitivity and specificity of the FMI dose error reconstruction was demonstrated for this 10% action level. Similar numbers were found for action levels of 5% and 20% γ failure. These results support the use of the FMI dose error algorithm for real-time 4D treatment verification.

The immediate purpose of the algorithm is to avoid gross treatment errors. Thus, if the action level is exceeded, the treatment could be halted either automatically or by the operator. Alternatively, a beam hold could be applied until the error level (calculated on a would-be dose increment) is again lower than the action level. For non-tracking treatments, such a scenario would correspond to what might be called dose-based gating, i.e. gating where the decision of triggering the beam on and off is based on dosimetric deviation. This approach would be more clinically relevant than the current clinically used gating scheme where the triggering of the beam is instead based on geometric displacement. While dose errors were induced by motion in the present study, errors of the same dosimetric magnitude due to other origins, e.g. MLC errors, can also be picked up by the algorithm.

Computational speed is important for many dose calculation algorithms (Vassiliev *et al* 2010, Men *et al* 2009, Ziegenhein *et al* 2013, Hissoiny *et al* 2011) and crucial for algorithms intended for real-time intrafractional use. We believe that the present temporal resolution of approximately 500 ms would be

sufficient for online real-time monitoring of dose error evolution during treatment delivery, and comparable resolutions in dose pulses and time were indeed also used in a recent study of real-time verification of superficial doses (Jarvis *et al* 2014). Online use of the FMI dose error algorithm should therefore be possible since it computed cumulative dose and evaluated cumulative errors in dose in several hundred points by γ failure rates in 36 ms + 259 ms, i.e. well below the temporal resolution of the dose data presented here. To reduce computation time further, the motion-induced dose errors could instead be quantified by the χ-formalism (Bakai *et al* 2003).

Online use of the FMI dose error algorithm would allow continuous feedback of the correctness of the dose in key target positions, the treated region as a whole, or any desired distribution of positions in real time during beam delivery. The decoupling of calculation points from voxels natively supports the utilization of patient specific monitoring without restrictions on spatial resolution or requirements of calculation in positions that are of less importance (Lu 2010, Dua and Srinivasan 2008). Furthermore, since motions can be applied separately for each calculation point, inclusion of time dependent rotations and deformations is also possible.

Alternative use of an online dose error calculation could be on-the-fly repair of erroneous dose delivery in MLC tracking treatments, where knowledge of errors in the present cumulative dose is used online when fitting the MLC leaves to the current target position. Knowledge of hitherto accumulated dose errors in a specific volume could be a help when deciding the best option of

opening or closing an MLC leaf during MLC tracking. Another alternative use could be integration of the FMI dose algorithm with an MLC tracking simulator (Poulsen *et al* 2013). This would enable dosimetric evaluation of MLC tracking with large sets of treatment plans and target motions that are practically beyond reach of time-consuming phantom experiments. Such large scale simulations have great potential for pre-treatment QA of MLC tracking, evaluations of tracking robustness for specific plans, investigation of tracking system designs, and for scientific studies of the clinical benefit of tracking.

While the FMI algorithm provided good estimations of dose error, the dose itself was subject to some uncertainty. The higher spread of dose differences in the penumbra is likely due to random imperfections in the alignment of the phantom and the aperture, e.g. because of noise in the target localization signal. However, due to the high dose gradient in the penumbra, such large dose differences as seen in Figure 2 may be generated by small spatial offsets. The mean dose difference between measured and reconstructed doses was within 1% for both moving and static targets but with a large standard deviation of up to 8%, which is poor compared to recent dose reconstruction algorithms (Vassiliev *et al* 2010, Nelms *et al* 2012, Poulsen *et al* 2012b). The algorithm overestimated the dose in high dose regions while underestimating the dose in low dose regions. This is in part due to less smearing of the dose in the reconstructions than in the measurements, owing to the truncated SPB kernel. Furthermore, the dose in high dose regions was overestimated because the field size in the algorithm was fixed to 10×10 cm^2, thereby ignoring changing

output factors and PDD shapes with field size. The lung plans, for instance, had considerably smaller field sizes (5×5 cm^2 or less). Underestimation of dose in low dose regions is also seen in other studies using PBC algorithms (Belec and Clark 2013). Using an SPB kernel at just a single depth means that the part of penumbra widening that comes from phantom scatter is not modelled – only the penumbra widening due to beam divergence is modelled. The missing correction for surface obliqueness is negligible close to the central axis but adds additional uncertainty in the periphery of the phantom. The plans used here were sufficiently confined to the central part of the phantom to be negligibly affected. Also, the gantry-dependent attenuation is not equal for all diodes as assumed in the attenuation correction factor, which again adds to the uncertainty of the reconstruction.

A notable source of uncertainty may be found in the simplicity of the density correction, and, although not a problem for the homogeneous phantom used here, doses should be considered with due care for inhomogeneous objects. It is an obvious limitation that the FMI algorithm only reconstructs doses and dose errors to the homogeneous Delta4PT phantom and not to the patient. Therefore, the FMI reconstructed doses and dose errors may not be completely coherent with those actually occurring in the patient, especially for radiation to highly inhomogeneous tumour sites, such as the thorax. It is, however, in accordance with common QA procedure to measure both lung and prostate plans using a homogeneous phantom (Bedford *et al* 2009, Sadagopan *et al* 2009, Chandraraj *et al* 2011), and in line with 3D reconstructions of dose to a water-

filled body using *in vivo* portal dosimetry for inhomogeneous tumour sites (Wendling *et al* 2012, Mans *et al* 2010a). It is also in line with other work linking motion-induced dose perturbations in a patient with those in a homogeneous phantom (Feygelman *et al* 2013, Stambaugh *et al* 2013). In essence, the FMI dose error reconstruction provides the same kind of plan deliverability measure as the standard pre-treatment QA performed in our clinic using the Delta4PT dosimeter, but allows in-treatment use during irradiation and inclusion of target motion, as was the intention of the immediate study.

Clinical implementation of real-time FMI would require fast access to machine parameters and targets positions during treatment delivery and, preferably, porting of the code to a faster programming language in a standalone package that is more suitable in a clinical environment than the current Matlab implementation. Besides an online implementation, future development will work towards a refined FMI algorithm that provides more exact dose reconstruction calculated for the actual patient anatomy. Potential improvements of the algorithm could be to include PDDs and output factors of different field sizes, or avoiding truncation of the scatter kernel, which may require Fast-Fourier Transform convolution to uphold similar computational speed. Surface obliqueness can also be approximated at relatively little computational cost, which leaves scatter as a function of depth and fast inhomogeneity correction as the remaining major challenges for computing actual dose to inhomogeneous tumour sites in real time.

In the meantime, the presented FMI dose error algorithm may expand current clinical phantom-based QA procedures to real-time intrafractional use with inclusion of motion. This is particularly important for MLC tracking where neither the target motion nor the MLC movements are known beforehand. While accurate reconstruction of dose is crucial for planning and follow-up, the main interest during irradiation is how well the planned dose is being delivered, i.e. how much the actual cumulative dose looks like the intended cumulative dose. In other words, the FMI dose error reconstruction provides a good estimate of the main quantity of interest during irradiation. *In vivo* QA has also been demonstrated by portal dosimetry (Prabhakar 2013, van Elmpt *et al* 2009, Mans *et al* 2010b). However, these treatment verification techniques either do not include target motion, are not applicable in real time, or both. Motion-including 3D dose reconstructions have been made (Bol *et al* 2012, Azcona *et al* 2014), but are again not applicable on a real-time scale. To our knowledge, the FMI algorithm is the first method feasible for 4D motion-including dose (error) reconstruction in real time. Although this study focused on MLC tracking, the FMI algorithm is also directly applicable for other types of tracking on a standard linear accelerator, such as couch tracking (D'Souza *et al* 2005).

Conclusions

A fast motion-including dose reconstruction algorithm was created. Its ability to reproduce motion-induced dose errors, similar to those of a standard pre-treatment QA tool throughout beam delivery, was validated experimentally

for VMAT treatments with and without MLC tracking. While absolute doses are subject to some uncertainty, the FMI dose error reconstruction allows accurate temporal and spatial pinpointing of errors in the dose delivered to moving targets that could be due to both target motion and erroneous motion or behaviour of linear accelerator parts. The computation speed of the algorithm makes it feasible for real-time use. With an online implementation, it may be used for treatment intervention in case of erroneous dose delivery in both tracking and non-tracking treatments. Apart from being well suited for intrafractional QA, the FMI dose error algorithm may be used for large scale studies of motion-induced dose error and evaluations of MLC tracking plans pending development of an MLC tracking simulator.

Acknowledgements:

We gratefully thank Patrick Kupelian (University of California, Los Angeles) and Katja Langen (University of Maryland) for the prostate trajectories, Yelin Suh (MD Anderson Cancer Center) and Sonja Dieterich (University of California, Davis) for the lung tumor trajectories, Görgen Nilsson and Peter Münger (Scandidos) for fruitful discussions and modifications of the Delta4PT software to allow export of time-resolved dose data, Roman Iustin and Andreas Bergqvist (Micropos Medical AB) for modifications of the RayPilot system to allow integration with the tracking program, and Ann van Esch (7Sigma) and Lone Hoffmann (Aarhus University Hospital) for help with internals of the Varian Eclipse system.

This work was supported by The Danish Cancer Society, CIRRO (The Lundbeck Foundation Center for Interventional Research in Radiation Oncology), The Danish Council for Strategic Research, NCI Grant R01CA93626, and Varian Medical Systems.

Conflicts of interest

Aarhus University Hospital, Denmark, received financial support through a research agreement with Varian Medical Systems, Palo Alto, CA.

References

Azcona J D, Xing L, Chen X, Bush K and Li R 2014 Assessing the dosimetric impact of real-time prostate motion during volumetric modulated arc therapy *Int. J. Radiat. Oncol. Biol. Phys.* **88** 1167–74

Bakai A, Alber M and Nüsslin F 2003 A revision of the γ-evaluation concept for the comparison of dose distributions *Phys. Med. Biol.* **48** 3543

Bedford J L, Lee Y K, Wai P, South C P and Warrington A P 2009 Evaluation of the Delta4 phantom for IMRT and VMAT verification *Phys. Med. Biol.* **54** N167–76

Belec J and Clark B G 2013 Monte Carlo calculation of VMAT and helical tomotherapy dose distributions for lung stereotactic treatments with intra-fraction motion *Phys. Med. Biol.* **58** 2807

Bharat S, Parikh P, Noel C, Meltsner M, Bzdusek K and Kaus M 2012 Motion-compensated estimation of delivered dose during external beam radiation therapy: Implementation in Philips' Pinnacle[sup 3] treatment planning system *Med. Phys.* **39** 437–43

Bol G H, Hissoiny S, Lagendijk J J W and Raaymakers B W 2012 Fast online Monte Carlo-based IMRT planning for the MRI linear accelerator *Phys. Med. Biol.* **57** 1375

Chandraraj V, Stathakis S, Manickam R, Esquivel C, Supe S S and Papanikolaou N 2011 Comparison of four commercial devices for RapidArc and sliding

window IMRT QA *J. Appl. Clin. Med. Phys.* **12** Online: http://www.jacmp.org/index.php/jacmp/article/view/3367

Crijns S P M, Raaymakers B W and Lagendijk J J W 2012 Proof of concept of MRI-guided tracked radiation delivery: tracking one-dimensional motion *Phys. Med. Biol.* **57** 7863

D'Souza W D, Naqvi S A and Yu C X 2005 Real-time intra-fraction-motion tracking using the treatment couch: a feasibility study *Phys. Med. Biol.* **50** 4021

Dua S and Srinivasan P 2008 A non-voxel based feature extraction to detect cognitive states in fMRI *30th Annual International Conference of the IEEE Engineering in Medicine and Biology Society, 2008. EMBS 2008* 30th Annual International Conference of the IEEE Engineering in Medicine and Biology Society, 2008. EMBS 2008 pp 4431–4

Van Elmpt W, Nijsten S, Petit S, Mijnheer B, Lambin P and Dekker A 2009 3D In Vivo Dosimetry Using Megavoltage Cone-Beam CT and EPID Dosimetry *Int. J. Radiat. Oncol.* **73** 1580–7

Feygelman V, Stambaugh C, Zhang G, Hunt D, Opp D, Wolf T K and Nelms B E 2013 Motion as a perturbation: Measurement-guided dose estimates to moving patient voxels during modulated arc deliveries *Med. Phys.* **40** 021708

Hissoiny S, Ozell B, Bouchard H and Després P 2011 GPUMCD: A new GPU-oriented Monte Carlo dose calculation platform *Med. Phys.* **38** 754–64

Jarvis L A, Zhang R, Gladstone D J, Jiang S, Hitchcock W, Friedman O D, Glaser A K, Jermyn M and Pogue B W 2014 Cherenkov Video Imaging Allows for the First Visualization of Radiation Therapy in Real Time *Int. J. Radiat. Oncol.* **89** 615–22

Keall P J, Colvill E, O'Brien R, Ng J A, Poulsen P R, Eade T, Kneebone A and Booth J T 2014 The first clinical implementation of electromagnetic transponder-guided MLC tracking *Med. Phys.* **41** 020702

Keall P J, Kini V R, Vedam S S and Mohan R 2001 Motion adaptive x-ray therapy: a feasibility study *Phys. Med. Biol.* **46** 1–10

Keall P J, Mageras G S, Balter J M, Emery R S, Forster K M, Jiang S B, Kapatoes J M, Low D A, Murphy M J, Murray B R, Ramsey C R, Van Herk M B, Vedam S S, Wong J W and Yorke E 2006 The management of respiratory motion in radiation oncology report of AAPM Task Group 76 *Med. Phys.* **33** 3874–900

Keall P J, Sawant A, Cho B, Ruan D, Wu J, Poulsen P, Petersen J, Newell L J, Cattell H and Korreman S 2011 Electromagnetic-Guided Dynamic Multileaf Collimator Tracking Enables Motion Management for Intensity-Modulated Arc Therapy *Int. J. Radiat. Oncol.* **79** 312–20

Korreman S S 2012 Motion in radiotherapy: photon therapy *Phys. Med. Biol.* **57** R161

Krauss A, Nill S, Tacke M and Oelfke U 2011 Electromagnetic Real-Time Tumor Position Monitoring and Dynamic Multileaf Collimator Tracking Using a Siemens 160 MLC: Geometric and Dosimetric Accuracy of an Integrated System *Int. J. Radiat. Oncol.* **79** 579–87

Lee L, Le Q T and Xing L 2008 Retrospective IMRT dose reconstruction based on cone-beam CT and MLC log-file *Int. J. Radiat. Oncol. Biol. Phys.* **70** 634–44

Litzenberg D W, Moran J M and Fraass B A 2002 Verification of dynamic and segmental IMRT delivery by dynamic log file analysis *J. Appl. Clin. Med. Phys. Am. Coll. Med. Phys.* **3** 63–72

Liu Y, Shi C, Lin B, Ha C S and Papanikolaou N 2009 Delivery of four-dimensional radiotherapy with TrackBeam for moving target using an AccuKnife dual-layer MLC: dynamic phantoms study *J. Appl. Clin. Med. Phys.* **10** 2926–46

Low D A, Harms W B, Mutic S and Purdy J A 1998 A technique for the quantitative evaluation of dose distributions *Med. Phys.* **25** 656–61

Lu W 2010 A non-voxel-based broad-beam (NVBB) framework for IMRT treatment planning *Phys. Med. Biol.* **55** 7175

Malinowski K, Noel C, Lu W, Lechleiter K, Hubenschmidt J, Low D and Parikh P 2007 Development of the 4D Phantom for patient-specific, end-to-end radiation therapy QA *Proceedings of SPIE* Medical Imaging 2007: Physics of Medical Imaging vol 6510 (San Diego, CA, USA) p 65100E – 65100E – 9

Mans A, Remeijer P, Olaciregui-Ruiz I, Wendling M, Sonke J-J, Mijnheer B, van Herk M and Stroom J C 2010a 3D Dosimetric verification of volumetric-modulated arc therapy by portal dosimetry *Radiother. Oncol.* **94** 181–7

Mans A, Wendling M, McDermott L N, Sonke J-J, Tielenburg R, Vijlbrief R, Mijnheer B, Herk M van and Stroom J C 2010b Catching errors with in vivo EPID dosimetry *Med. Phys.* **37** 2638–44

Mayneord W V and Lamerton L F 1941 A Survey of Depth Dose Data *Br. J. Radiol.* **14** 255–64

McQuaid D and Webb S 2006 IMRT delivery to a moving target by dynamic MLC tracking: delivery for targets moving in two dimensions in the beam's eye view *Phys. Med. Biol.* **51** 4819–39

Men C, Gu X, Choi D, Majumdar A, Zheng Z, Mueller K and Jiang S B 2009 GPU-based ultrafast IMRT plan optimization *Phys. Med. Biol.* **54** 6565

Nelms B E, Opp D, Robinson J, Wolf T K, Zhang G, Moros E and Feygelman V 2012 VMAT QA: Measurement-guided 4D dose reconstruction on a patient *Med. Phys.* **39** 4228–38

Otto K 2008 Volumetric modulated arc therapy: IMRT in a single gantry arc *Med. Phys.* **35** 310–7

Poulsen P R, Fledelius W, Cho B and Keall P 2012a Image-Based Dynamic Multileaf Collimator Tracking of Moving Targets During Intensity-Modulated Arc Therapy *Int. J. Radiat. Oncol.* **83** e265–71

Poulsen P R, Ravkilde T, O'Brien R T and Keall P J 2013 Experimentally Validated Simulator of Dynamic MLC Tracking Treatments: A Tool for Tracking QA *Int. J. Radiat. Oncol. Biol. Phys.* **87** S45–S45

Poulsen P R, Schmidt M L, Keall P, Worm E S, Fledelius W and Hoffmann L 2012b A method of dose reconstruction for moving targets compatible with dynamic treatments *Med. Phys.* **39** 6237–46

Prabhakar R 2013 Real-time dosimetry in external beam radiation therapy *World J. Radiol.* **5** 352–5

Ravkilde T, Keall P J, Grau C, Høyer M and Poulsen P R 2013a Time-resolved dose distributions to moving targets during volumetric modulated arc therapy with and without dynamic MLC tracking *Med. Phys.* **40** 111723

Ravkilde T, Keall P J, Grau C, Høyer M and Poulsen P R 2013b Time-resolved dose reconstruction by motion encoding of volumetric modulated arc therapy fields delivered with and without dynamic multi-leaf collimator tracking *Acta Oncol.* **52** 1497–503

Ravkilde T, Keall P J, Højbjerre K, Fledelius W, Worm E and Poulsen P R 2011 Geometric accuracy of dynamic MLC tracking with an implantable wired electromagnetic transponder *Acta Oncol.* **50** 944–51

Sadagopan R, Bencomo J A, Martin R L, Nilsson G, Matzen T and Balter P A 2009 Characterization and clinical evaluation of a novel IMRT quality assurance system *J. Appl. Clin. Med. Phys.* **10**

Sawant A, Dieterich S, Svatos M and Keall P 2010 Failure mode and effect analysis-based quality assurance for dynamic MLC tracking systems *Med. Phys.* **37** 6466–79

Sawant A, Venkat R, Srivastava V, Carlson D, Povzner S, Cattell H and Keall P 2008 Management of three-dimensional intrafraction motion through real-time DMLC tracking *Med Phys* **35** 2050–61

Stambaugh C, Nelms B E, Dilling T, Stevens C, Latifi K, Zhang G, Moros E and Feygelman V 2013 Experimentally studied dynamic dose interplay does not meaningfully affect target dose in VMAT SBRT lung treatments *Med. Phys.* **40** 091710

Storchi P R M, Battum L J van and Woudstra E 1999 Calculation of a pencil beam kernel from measured photon beam data *Phys. Med. Biol.* **44** 2917–28

Storchi P and Woudstra E 1995 Calculation models for determining the absorbed dose in water phantoms in off-axis planes of rectangular fields of open and wedged photon beams *Phys. Med. Biol.* **40** 511–27

Storchi P and Woudstra E 1996 Calculation of the absorbed dose distribution due to irregularly shaped photon beams using pencil beam kernels derived from basic beam data *Phys. Med. Biol.* **41** 637–56

Thomas S J 1999 Relative electron density calibration of CT scanners for radiotherapy treatment planning *Br. J. Radiol.* **72** 781–6

Vassiliev O N, Wareing T A, McGhee J, Failla G, Salehpour M R and Mourtada F 2010 Validation of a new grid-based Boltzmann equation solver for dose calculation in radiotherapy with photon beams *Phys. Med. Biol.* **55** 581

Wendling M, McDermott L N, Mans A, Olaciregui-Ruiz Í, Pecharromán-Gallego R, Sonke J-J, Stroom J, Herk M van and Mijnheer B J 2012 In aqua vivo EPID dosimetry *Med. Phys.* **39** 367–77

Yu C X 1995 Intensity-modulated arc therapy with dynamic multileaf collimation: an alternative to tomotherapy *Phys. Med. Biol.* **40** 1435–49

Ziegenhein P, Kamerling C P, Bangert M, Kunkel J and Oelfke U 2013 Performance-optimized clinical IMRT planning on modern CPUs *Phys. Med. Biol.* **58** 3705